J Mater Sci (2026) 61:10421–10434

Energy materials

Two structural transformation mechanisms of ZIF-8 induced by encapsulation of imidazolium-based aprotic ionic liquids

Wen Yang[1,2], Christian Rodenbücher[1], Jiangshui Luo[3,*], and Carsten Korte[1,*]

[1] *Institute of Energy Technologies (IET-4), Forschungszentrum Jülich GmbH, Jülich, Germany*
[2] *Faculty of Mathematics, Computer Science and Natural Sciences, RWTH Aachen University, Aachen, Germany*
[3] *College of Materials Science and Engineering, Sichuan University, Chengdu, China*

Received: 21 November 2025
Accepted: 28 January 2026
Published online: 25 February 2026

ABSTRACT

Metal–organic frameworks (MOFs) are three-dimensional crystalline materials composed of metal nodes and organic ligands, forming porous coordination networks with high surface areas and tunable internal cavities. These structural features enable MOFs to act as hosts for small guest molecules, such as ionic liquids (ILs), facilitating host–guest interactions that can modify physical properties and enhance performance in applications such as fuel cells and batteries. In this study, two imidazolium-based aprotic ILs with different anions, 1-ethyl-3-methylimidazolium trifluoromethanesulfonate ([Emim][TfO]) and 1-ethyl-3-methylimidazolium bis-(trifluoromethylsulfonyl)imide ([Emim][TFSI]), were successfully encapsulated within the pores of the MOF ZIF-8. The structural and vibrational impacts of these ILs on the ZIF-8 framework were systematically investigated using powder X-ray diffraction (PXRD) and Fourier-transform infrared spectroscopy (FT-IR). The results revealed two distinct mechanisms for the uptake of an IL, leading to an expansion of the MOF cage structure: [Emim][TfO]@ZIF-8 exhibited a phase transition characterized by the coexistence of two lattice constants, while [Emim][TFSI]@ZIF-8 maintained a single-phase structure with continuous lattice expansion upon increased loading. These behaviors are attributed to the swing motion of 2-methylimidazole linkers and the elongation of Zn–N bonds induced by internal pressure from the confined ILs. Additionally, confinement within the ZIF-8 cages led to the strengthening of $-SO_3$ and S–N–S bonds in the ILs, as evidenced by the blue-shifted and intensified IR vibrational modes. This study provides fundamental insights into the structural evolution and host–guest interactions in IL@MOF systems, offering guidance for tailoring MOF properties through ILs encapsulation.

Handling Editor: Ivo Teixeira.

Address correspondence to E-mail: jiangshui.luo@scu.edu.cn; c.korte@fz-juelich.de

https://doi.org/10.1007/s10853-026-12380-0

Introduction

MOFs are a class of hierarchical materials with tunable pore sizes across multiple length scales [1]. These materials are constructed from metal ions or clusters, commonly including copper, zinc, iron, aluminum, and chromium, coordinated to organic linkers such as carboxylates, imidazolates, amines, and pyridyl groups [2]. The resulting framework forms an extended polymeric network characterized by high porosity and an exceptionally large surface area. MOFs exhibit various intermolecular interactions, including coordination bonds, electrostatic attractions between metal centers and ligands, π–π stacking between aromatic rings, van der Waals forces between nonpolar regions, and hydrogen bonding with neighboring molecules [3–5]. The pore size and geometry of MOFs can be precisely tuned for specific applications by altering the metal nodes and organic linkers during synthesis [6]. These porous crystalline materials offer high internal surface areas, large pore volumes, and excellent storage capacity, making them promising candidates for applications in gas separation, catalysis, drug delivery, fuel cells, and batteries.

ILs are salts composed of bulky organic cations and large anions of superacids (*e.g.* $[TfO]^-$, $[TFSI]^-$, $[BF_4]^-$, $[PF_6]^-$), resulting in a low lattice energy. This results in low melting points, and thus, ILs remain in the liquid state at or below a defined temperature, typically around 100 °C [7]. ILs can be broadly classified into two categories: protic ionic liquids (PILs) and aprotic ionic liquids (AILs) [8, 9]. PILs contain acidic (active) protons, such as $–NH^+$ or –OH groups, which can participate in extensive hydrogen bonding networks [10, 11]. PILs with an acidic cation $[HB]^+[A]^-$ are synthesized via proton transfer reactions between a Brønsted acid HA and a Brønsted base B. This feature enables proton conductivity, making PILs particularly useful for applications such as proton exchange membranes in fuel cells and acidic catalysis. AILs, on the other hand, are composed of (quaternized) organic cations (*e.g.* alkylammonium, imidazolium, pyridinium, etc.) usually prepared by alkylation (S_N2) reactions that do not possess transferable protons [12, 13]. As such, AILs lack significant hydrogen-bonding capabilities and do not support proton conduction. However, their high thermal and chemical stability, low volatility, and broad electrochemical windows make them ideal for applications in supercapacitors, lithium-ion batteries, lubricants, and green solvents for synthesis and separation processes [14].

Confining AILs within the micropores of MOFs has emerged as a promising research direction, particularly due to the enhanced performance of these hybrid materials in applications such as energy storage and conversion. The incorporation of guest molecules into the porous architecture of MOFs is governed by host–guest interactions, which are typically non-covalent in nature, involving electrostatic forces, hydrogen bonding, van der Waals interactions, or π–π stacking between the guest species and the MOF framework. For instance, Dehdashtian et al. reported the successful synthesis of a chromium-based MOF (MIL-101) loaded with 1-hexyl-3-methylimidazolium chloride, which was employed as a working electrode in the development of an electrochemical sensor [15]. Zhang et al. fabricated a surface-mounted HKUST-1 ($Cu_3(BTC)_2(H_2O)_3$, BTC = 1,3,5-benzenetricarboxylate) MOF loaded with 1-butyl-3-methylimidazolium bis(trifluoromethylsulfonyl)imide ([Bmim][TFSI]) to investigate ionic conductivity for further application in energy storage application, for example, electrolyte for battery [16]. Su et al. incorporated two types of IL, 1,3-dimethylimidazolium tetrafluoroborate and 1-allyl-3-methylimidazolium dicyanamide, in the MOF MIL-101. The ionic conductivity of the composite electrolyte can reach values as high as 3.73×10^{-3} S cm^{-1}, and it is regarded as a fast ionic conductor due to its low activation energy (< 0.4 eV) [17]. These findings revealed the promising electrochemical performance of MOF@AIL systems and the importance of understanding the fundamental interactions between MOF cages and AIL ions. Gaining deeper insight into these host–guest interactions is crucial for the rational design and optimization of hybrid materials for next-generation energy storage and conversion technologies.

In this study, ZIF-8 (Basolite®), a zinc-based three-dimensional metal–organic framework, was chosen as the model MOF due to its high thermal stability and well-defined crystallinity. ZIF-8 is a 2-methylimidazole zinc salt, *i.e.* $Zn^{2+}(CH_3C_4H_2N_2^-)_2$. It has a cubic ($I\bar{4}3m$) zeolite-type structure with 2 sodalite cages per unit cell and a lattice constant $a = 16.9956(12)$ Å [18]. The selected guest compounds were two imidazolium-based AILs, 1-ethyl-3-methylimidazolium bis-(trifluoromethylsulfonyl)imide ([Emim][TFSI]) and 1-ethyl-3-methylimidazolium trifluoromethanesulfonate ([Emim][TfO]). Both AILs are widely utilized

in electrochemical applications for their excellent ionic conductivity and thermal stability [19, 20]. The objective of this work is to investigate the molecular interactions between these AILs and the cage structure of ZIF-8, with a particular emphasis on possible phase transitions and changes of the host and guest molecular vibration modes induced by the AIL encapsulation. To investigate these host–guest interactions, a series of comprehensive structural characterizations were performed. PXRD was used to monitor changes in crystal structure and phase behavior, IR provided insights into variations in bonding environments and functional group interactions, and Brunauer–Emmett–Teller (BET) surface area analysis was conducted to evaluate porosity and surface area changes upon IL incorporation.

Experiment

Materials

ZIF-8 MOF (Zeolitic imidazolate framework-8, Basolite® Z1200) was purchased from Merck KGaA. 1-Ethyl-3-methylimidazolium bis-(trifluoromethylsulfonyl)imide ([Emim][TFSI]) and 1-Ethyl-3-methylimidazolium trifluoromethanesulfonate ([Emim][TfO]) were purchased from Sigma-Aldrich Co. (USA). Before use, all the AILs were washed with ethyl acetate three times and then vacuum-dried over 10 h at 60 °C.

Preparation of IL@MOF

The synthesis of [Emim][TfO]@ZIF-8 and [Emim][TFSI]@ZIF-8 was carried out through the capillary action method (Fig. 1). The quantity ratios of [Emim][TfO] molecules to ZIF-8 cages were as follows: 1.93:1, 3.87:1, 5.80:1, 7.74:1, and 9.67:1 calculated according to Eq. S1–S5. As indicated in Table 1, these ratios were determined to correspond to the theoretical pore volume of ZIF-8 at loadings of 20%, 40%, 60%, 80%, and 100%, respectively. Similarly, the quantity ratios of [Emim][TFSI] ion pairs to ZIF-8 cages were as follows: 1.39:1, 2.78:1, 4.16:1, 5.55:1, and 6.94:1, as indicated in Table 2. These calculations were executed according to equations S1 through S5. The volume occupancy was derived from the pore volume measurement of ZIF-8 (0.663 cm^3/g), as determined through BET analysis. In a typical synthesis procedure, 66.3 μL of [Emim][TfO] and 100 mg of dehydrated ZIF-8 were thoroughly mixed using a mortar and pestle. Subsequently, the resulting powders were subjected to overnight drying under vacuum conditions at 105 ℃. This particular sample was denoted as $ET_{9.67}$@Z, which signifies the combination of 66.3 μL [Emim][TfO] with 100 mg ZIF-8. A similar procedure was applied to prepare samples designated as ET_x@Z, where x values corresponded to 1.93, 3.87, 5.80, 7.74, and 9.67. Likewise, [Emim]

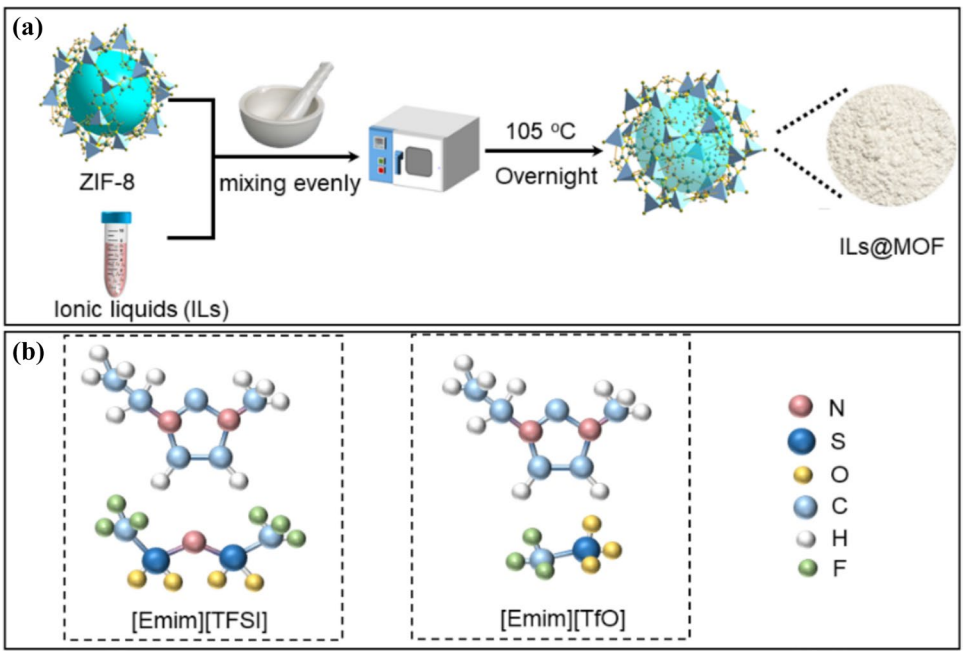

Figure 1 **a** Workflow of the synthesis process in this study, **b** schematic representation of the two selected AILs' ion pairs

Table 1 Components of [Emim][TfO]@ZIF-8 composites in this study

Sample	[Emim][TfO]/µL	ZIF-8/mg	Occupied pore volume ratio/%	Quantity ratio ([Emim][TfO] molecules: ZIF-8 cages)
ZIF-8	0	100	0	0:1
$ET_{1.93}$@Z	13.26	100	20	1.93:1
$ET_{3.87}$@Z	26.52	100	40	3.87:1
$ET_{5.80}$@Z	39.78	100	60	5.80:1
$ET_{7.74}$@Z	53.04	100	80	7.74:1
$ET_{9.67}$@Z	66.30	100	100	9.67:1

Table 2 Components of [Emim][TFSI]@ZIF-8 composites in this study

Sample	[Emim][TFSI]/µL	ZIF-8/mg	Occupied pore volume ratio/%	Quantity ratio ([Emim][TFSI] ion pairs: ZIF-8 cages)
ZIF-8	0	100	0	0:1
$EI_{1.39}$@Z	13.26	100	20	1.39:1
$EI_{2.78}$@Z	26.52	100	40	2.78:1
$EI_{4.16}$@Z	39.78	100	60	4.16:1
$EI_{5.55}$@Z	53.04	100	80	5.55:1
$EI_{6.94}$@Z	66.30	100	100	6.94:1

[TFSI]@ZIF-8 was referred to as EI_x@Z, where x values corresponded to 1.39, 2.78, 4.16, 5.55, and 6.94.

Characterization

Nitrogen adsorption and desorption isotherms were conducted at 77 K, utilizing the Micromeritics' Gemini VII instrument (Georgia, USA). PXRD patterns of the samples were obtained with a Bruker D8 Advanced Diffraction instrument (Karlsruhe, Germany), employing CuK_α radiation ($\lambda = 0.15418$ nm). The diffractogram was further analyzed using Rietveld refinement using Profex software [21] to evaluate the effects of AIL molecules on crystal properties such as lattice parameters. IR analyses were carried out with the GladiATRTM spectrometer (Madison, USA), covering the wavenumber range of 400 to 1600 cm^{-1}. All peak fitting operations and deconvolution were conducted using Fityk software [22].

Results

BET measurements

In Fig. 2, the nitrogen gas adsorption isotherms of the hybrid materials measured at 77 K are depicted. Pristine ZIF-8, [Emim][TfO]@ZIF-8 and [Emim][TFSI]@ZIF-8 exhibit type I isotherms, as expected for a microporous material like ZIF-8, see Fig. 2a and c. In Fig. 2b, the BET surface area of $ET_{1.93}$@Z, $ET_{3.87}$@Z, $ET_{5.80}$@Z, $ET_{7.74}$@Z, and $ET_{9.67}$@Z are plotted against the quantity ratio AIL ion pairs: ZIF-8 cages. The measured BET surface areas have values of 1059(16) m^2/g, 557(8) m^2/g, 274(5) m^2/g, 9.9(1) m^2/g, and 7.3(1) m^2/g. There is a significant decrease compared to the surface area of pristine ZIF-8 with a value of 1452(22) m^2/g. The pore volumes of $ET_{1.93}$@Z, $ET_{3.87}$@Z, $ET_{5.80}$@Z, $ET_{7.74}$@Z, and $ET_{9.67}$@Z reveal values of 4626(243) × 10^{-4} cm^3/g, 2436(181) × 10^{-4} cm^3/g, 1284(153) × 10^{-4} cm^3/g, 150(12) × 10^{-4} cm^3/g, and 4.3(2) × 10^{-4} cm^3/g, respectively. These values differ from the pore volume measure for pristine ZIF-8, which has a value of 6630(89) × 10^{-4} cm^3/g. According to these results, the pores of ZIF-8 are completely occupied when intercalating about 7 [Emim][TfO] ion pairs into a ZIF-8 sodalithe cage.

The BET surface area of $EI_{1.39}$@Z, $EI_{2.78}$@Z, $EI_{4.16}$@Z, $EI_{5.55}$@Z, and $EI_{6.94}$@Z is shown in Fig. 1d. Values of 756(11) m^2/g, 634(8) m^2/g, 30(2) m^2/g, 2.8(1) m^2/g, and 0.57(5) m^2/g can be measured, respectively. Again, the BET surface area significantly decreases when comparing to the surface area of pristine ZIF-8, which has a value of 1452(22) m^2/g. The same can be observed for

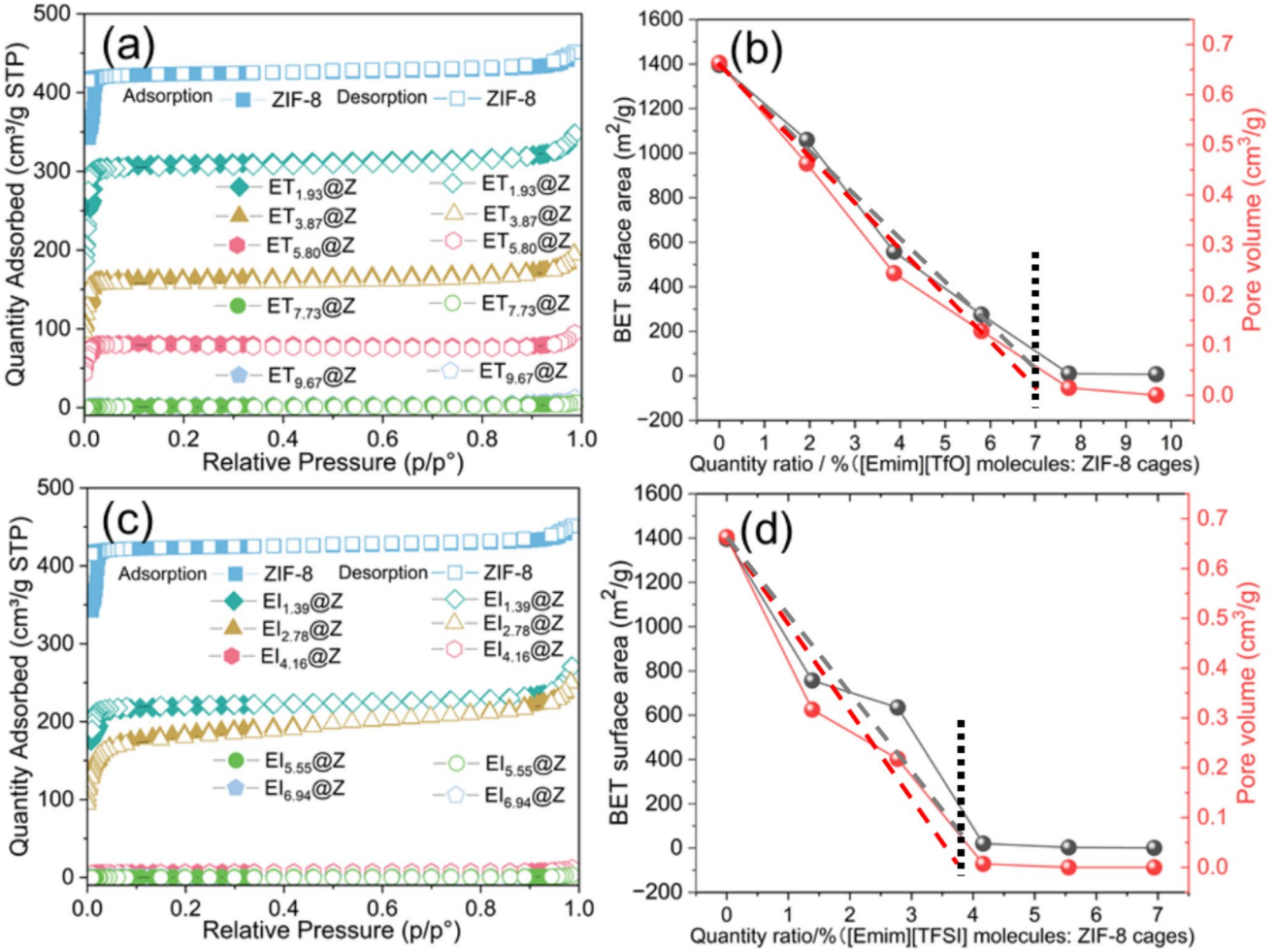

Figure 2 N_2 adsorption–desorption isotherms of (**a**) [Emim][TfO]@ZIF-8 and (**c**) [Emim][TFSI]@ZIF-8 at 77 K. Variation of BET specific surface and pore volume of (**b**) [Emim][TfO]@ZIF-8 and (**d**) [Emim][TFSI]@ZIF-8 with different quantity ratio of [Emim][TfO] molecules: ZIF-8 cages and [Emim][TFSI] molecules: ZIF-8 cages. (STP: Standard temperature and pressure)

the pore volume of $EI_{1.39}$@Z, $EI_{2.78}$@Z, $EI_{4.16}$@Z, $EI_{5.55}$@Z, and $EI_{6.94}$@Z, which exhibits values of $3166(192) \times 10^{-4}$ cm^3/g, $2177(123) \times 10^{-4}$ cm^3/g, $70(5) \times 10^{-4}$ cm^3/g, $1.3(1) \times 10^{-4}$ cm^3/g, and $0.32(1) \times 10^{-4}$ cm^3/g, respectively. The pore volume of pristine ZIF-8 has a value of 6423×10^{-4} cm^3/g. Thus, the pores of ZIF-8 became presumably completely occupied when intercalating 3.7 [Emim][TFSI] ion pairs into the sodalite cages.

XRD measurements

The results of the XRD investigations on the [Emim][TfO]@ZIF-8 and [Emim][TFSI]@ZIF-8 samples are shown in Fig. 3. The crystal structure refinement was performed by using Profex software, confirming that pristine ZIF-8 adopts a bcc structure with the space group $I\bar{4}3m$, as shown in Fig. S1 and S2 [21]. A value of 17.0230(2) Å is found for the lattice constant of pristine ZIF-8, see Fig. 4e and Table S1

The PXRD analysis of the [Emim][TfO]@ZIF-8 samples reveals the emergence of new diffraction peaks adjacent to the original ZIF-8 peaks, see Fig. 3a. Notably, the intensity of these new peaks is increasing with increasing [Emim][TfO] loading, while the original peaks gradually fade out. In contrast, the introduction of [Emim][TFSI] leads to a uniform leftward shift of all the original ZIF-8 XRD peaks, as can be seen in Fig. 3b. The diffraction peak corresponding to the (200) plane of pristine ZIF-8 is located at 12.92°, see Fig. 4a. Upon encapsulation of [Emim][TfO] within ZIF-8, the intensity of this original peak slightly decreases, while a new peak

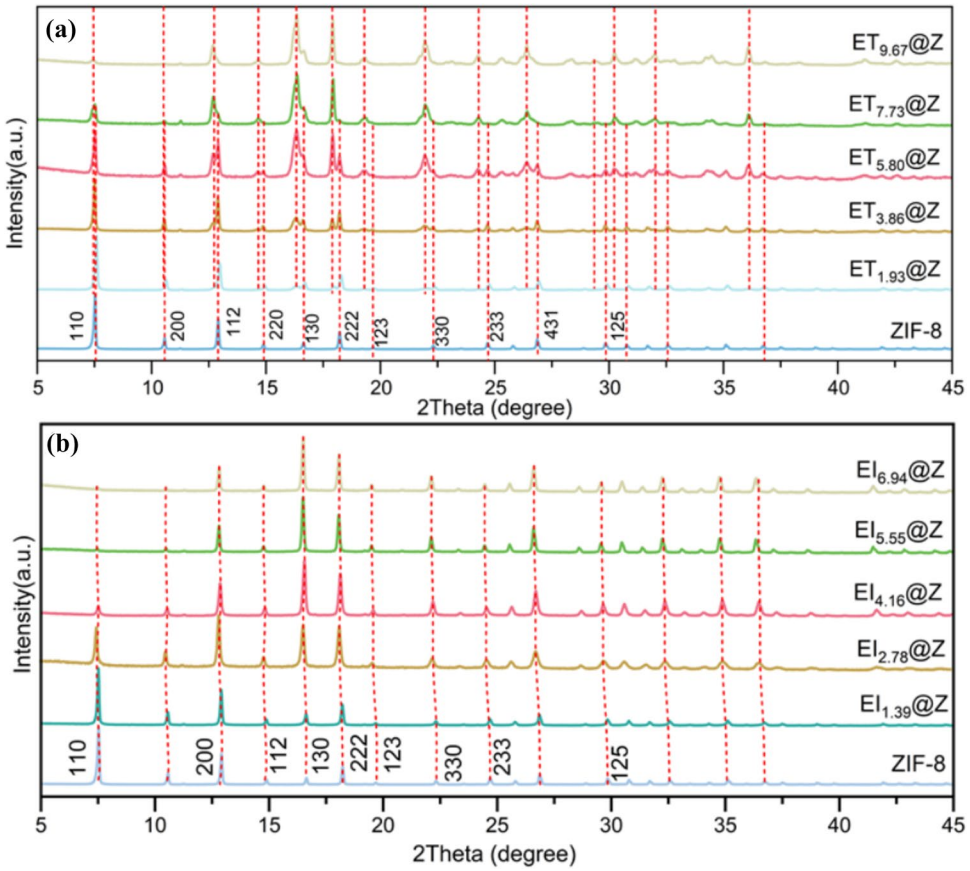

Figure 3 PXRD patterns of (**a**) [Emim][TfO]@ZIF-8 and (**b**) [Emim][TFSI]@ZIF-8

emerges to the left. With increasing [Emim][TfO] loading, the intensity of the original peak continues to decline, whereas the newly formed peak becomes more pronounced. Eventually, at higher loadings, the original peak disappears entirely, leaving only the new set of peaks. Furthermore, the area ratio of the newly formed peaks to the original peaks exhibits a linear relationship as a function of the molar ratio of [Emim][TfO] ion pairs to ZIF-8 cages, see Fig. 4c. The $ET_{9.67}$@Z sample retains the same crystal structure type as neat ZIF-8, but exhibits an expanded lattice with a lattice constant of 17.361(3) Å, representing an increase of 1.99% as shown in Fig. 4e. The other samples, including $ET_{1.93}$@Z, $ET_{3.87}$@Z, $ET_{5.80}$@Z, and $ET_{7.74}$@Z, exhibit a mixed-phase composition. The phase ratio evolves linearly with rising [Emim][TfO] content, as shown in Fig. 4c, reflecting a gradual phase transformation driven by AIL incorporation. No nucleation process occurs within the system. Instead, phase transfer is directly triggered by the encapsulation of [Emim][TfO] within the ZIF-8 cages, leading to physical expansion from the original cage. Both pristine ZIF-8 (original) and $ET_{9.67}$@Z (expanded) phases coexist in the samples $ET_{1.93}$@Z, $ET_{3.87}$@Z, $ET_{5.80}$@Z, and $ET_{7.74}$@Z, with the relative phase fractions varying across compositions.

In the case of the intercalation of [Emim][TFSI] in ZIF-8, the PXRD pattern reveals a continuous leftward shift of all peaks, as shown in Fig. 3b. For instance, the peak corresponding to the (200) planes of pristine ZIF-8, initially located at 12.92°, progressively shifts to lower angles with increasing [Emim][TFSI] loading, see Fig. 4b and d. The (200) peak positions are observed at 12.91°, 12.87°, 12.83°, 12.79°, and 12.78° for $EI_{1.39}$@Z, $EI_{2.78}$@Z, $EI_{4.16}$@Z, $EI_{5.55}$@Z, and $EI_{6.94}$@Z, respectively. The results of a crystal structure refinement of the [Emim][TFSI]@ZIF-8 samples confirm that the crystal structure type remains unchanged, preserving the bcc structure with the space group $I\bar{4}3m$. However, the lattice constant exhibits a systematic increase with increasing [Emim][TFSI] loading. As depicted in Fig. 4f, the lattice constants obtained for $EI_{1.39}$@Z, $EI_{2.78}$@Z, $EI_{4.16}$@Z, $EI_{5.55}$@Z and $EI_{6.94}$@Z are 17.0302(4) Å (+ 0.04%), 17.119(1) Å (+ 0.56%), 17.1641(8) Å

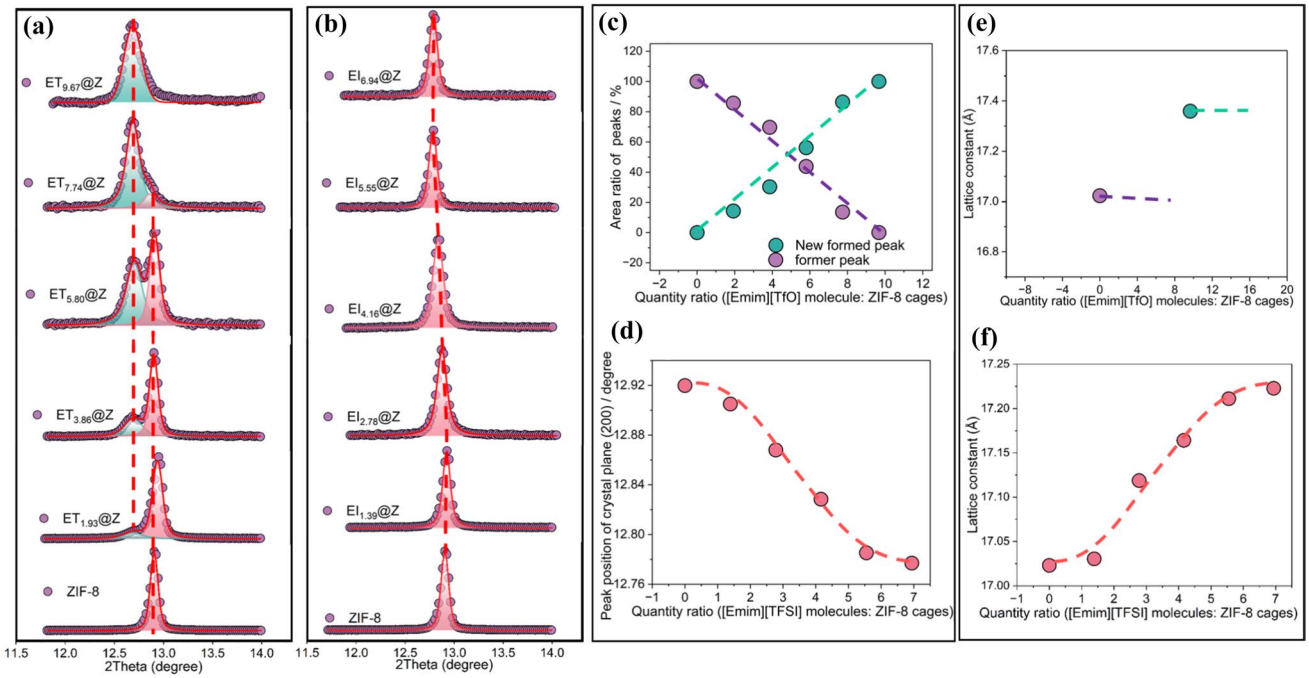

Figure 4 PXRD patterns of (**a**) [Emim][TfO]@ZIF-8 and (**b**) [Emim][TFSI]@ZIF-8 relating to (200) planes fitting by Fityk software, (**c**) the area ratio of newly formed peaks and original peaks relating to (200) planes in [Emim][TfO]@ZIF-8 as a function of quantity ratio ([Emim][TfO]: ZIF-8 cages), (**d**) peak position of (200) planes in [Emim][TFSI]@ZIF-8 as a function of quantity ratio ([Emim][TFSI]: ZIF-8 cages), (**e**) lattice constant of ZIF-8 and $ET_{9.67}$@Z, (**f**) lattice constant of [Emim][TFSI]@ZIF-8 as a function of quantity ratio ([Emim][TFSI]: ZIF-8 cages) refined by Profex software

(+ 0.83%), 17.2111(6) Å (+ 1.10%) and 17.223(1) Å (+ 1.17%), respectively. These results indicate a linear relationship between lattice expansion and [Emim][TFSI] loading.

IR measurements

Infrared spectroscopy was conducted to investigate the interactions occurring between the AILs and ZIF-8, evaluating the shifts in frequency and the broadening of peaks. The IR spectra were recorded for neat ZIF-8, [Emim][TfO], and [Emim][TFSI], as well as for ZIF-8 with varying amounts of intercalated [Emim][TfO] and [Emim][TFSI], as shown in Fig. 5a and b. The IR spectra of neat ZIF-8, [Emim][TfO], and [Emim][TFSI] were previously reported in the literature [23–25]. For [Emim][TfO]@ZIF-8, the band at 1027.4 cm^{-1}, corresponding to the asymmetric bending vibration mode $\delta_{as}(SO_2)$ of the triflate anion of [Emim][TfO], becomes sharper upon intercalation in the ZIF-8 pores, as shown in Fig. 6a. Upon entering the pores, the $\delta_{as}(SO_2)$ mode shifts to a higher wavenumber of 1030.2 cm^{-1} for $ET_{1.93}$@Z. As the [Emim][TfO] loading further increases, the mode gradually shifts again to lower wavenumbers. Specifically, the $\delta_{as}(SO_2)$ mode shifts to 1029.8 cm^{-1} for $ET_{3.87}$@Z and $ET_{5.80}$@Z, and further to 1029.3 cm^{-1} for $ET_{7.74}$@Z and $ET_{9.67}$@Z, as shown in Fig. 6b.

Similarly, for [Emim][TFSI]@ZIF-8, the band at 564.1 cm^{-1}, corresponding to the bending vibration mode δ(S–N-S) of [Emim][TFSI], becomes sharper upon encapsulation within the ZIF-8 pores, see Fig. 6c. Upon entering the pores, the δ(S–N-S) bending vibration mode shifts to a higher wavenumber of 573.2 cm^{-1} for $EI_{1.39}$@Z. As the [Emim][TFSI] loading further increases, the mode gradually shifts to lower wavenumbers. Explicitly, the δ(S–N-S) bending vibration mode shifts to 572.3 cm^{-1} for $EI_{2.78}$@Z, 571.3 cm^{-1} for $EI_{4.16}$@Z, 569.9 cm^{-1} for $EI_{5.55}$@Z and finally 569.4 cm^{-1} for $EI_{6.94}$@Z as shown in Fig. 6d.

The band at 420.4 cm^{-1}, corresponding to the stretching vibration ν(Zn-N) of the ZIF-8 skeleton, is shown in Fig. 5a and b. To analyze the shifts and intensity changes of this vibrational mode of the Zn-N bond upon AIL intercalation, peak fitting was performed using Fityk software for both [Emim]

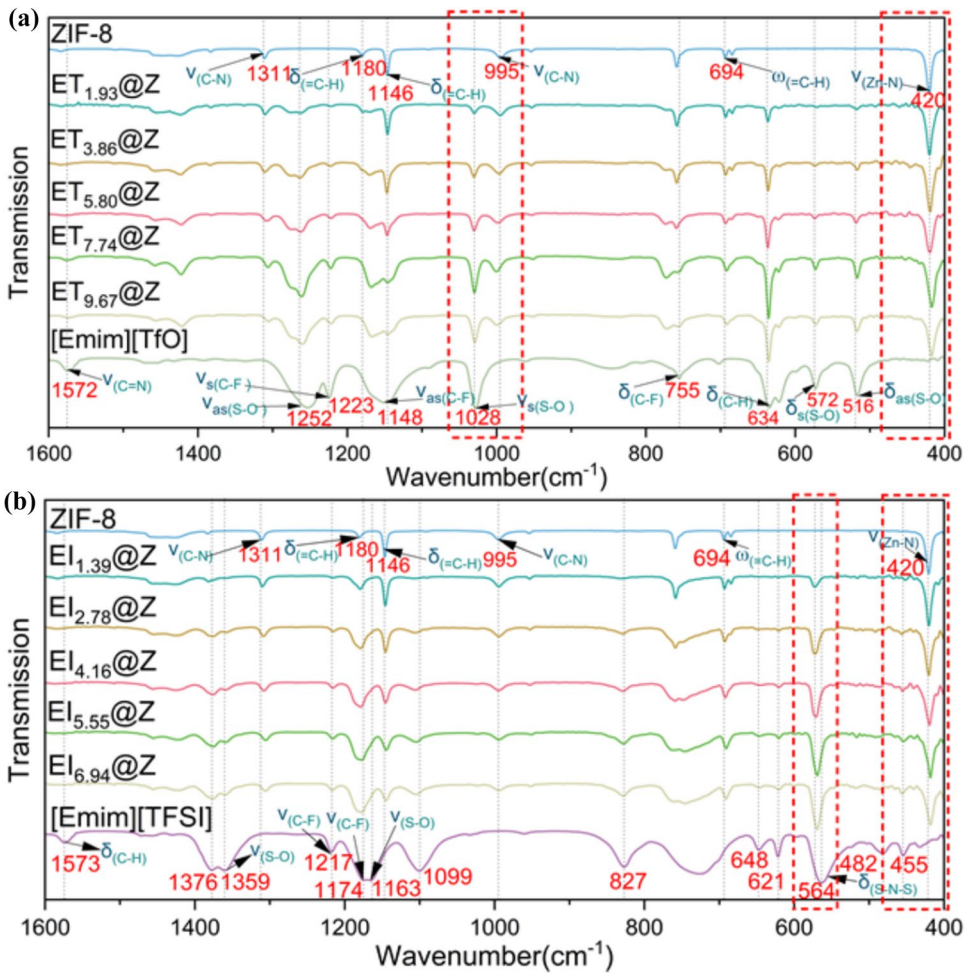

Figure 5 IR spectra of (**a**) [Emim][TfO]@ZIF-8 and **b** [Emim][TFSI] for 1600 cm^{-1} – 400 $cm.^{-1}$, IR spectra of (**c**) $\delta_{as(SO3)}$ from [Emim][TfO] and **d** $\delta_{(S-N-S)}$ from [Emim][TFSI]

[TfO]@ZIF-8 and [Emim][TFSI]@ZIF-8, see Fig. 7a and b. For [Emim][TfO]@ZIF-8, a newly formed peak appears at a lower wavenumber adjacent to the original peak, specifically at 417.9 cm^{-1}. For [Emim][TfO]@ZIF-8, the intercalation process results in a decrease in the intensity of the original ν(Zn-N) stretching mode, accompanied by an increase in the new peak at a lower wavenumber. At higher loadings for $ET_{9.67}$@Z, the original ν(Zn-N) mode disappears entirely, leaving only the newly formed peak as shown in Fig. 7c. For [Emim][TFSI]@ZIF-8, the intercalation of [Emim][TFSI] within the ZIF-8 cages induces a continuous shift of the ν(Zn-N) stretching vibration mode toward lower wavenumbers. As the [Emim][TFSI] loading increases, the wavenumber of the ν(Zn-N) stretching vibration mode decreases. Specifically, the ν(Zn-N) mode is observed at 419.9 cm^{-1}, 419.4 cm^{-1}, 418.9 cm^{-1}, 418.4 cm^{-1}, and 417.9 cm^{-1} for $EI_{1.39}$@Z, $EI_{2.78}$@Z, $EI_{4.16}$@Z, $EI_{5.55}$@Z, and $EI_{6.94}$@Z, respectively. The shift in wavenumber follows a linear trend with increasing [Emim][TFSI] loading as shown in Fig. 7d.

Discussion

In our study, we have successfully encapsulated two AILs, [Emim][TFSI] and [Emim][TfO], within the pores of ZIF-8. This encapsulation was confirmed by a noticeable decrease in the BET surface area and pore volume, demonstrating the effective occupation of the internal cavities by the AILs.

When the AILs are intercalated in the pores of ZIF-8, the vibrational characteristics of the specific chemical bonds are altered due to the confined environment imposed by the framework. In the case of [Emim][TfO], the IR band corresponding to the asymmetric bending vibration $\delta_{as}(SO_2)$ of the triflate anion shifts to a higher wavenumber. This shift is presumably attributed to the disruption of ion pair interactions

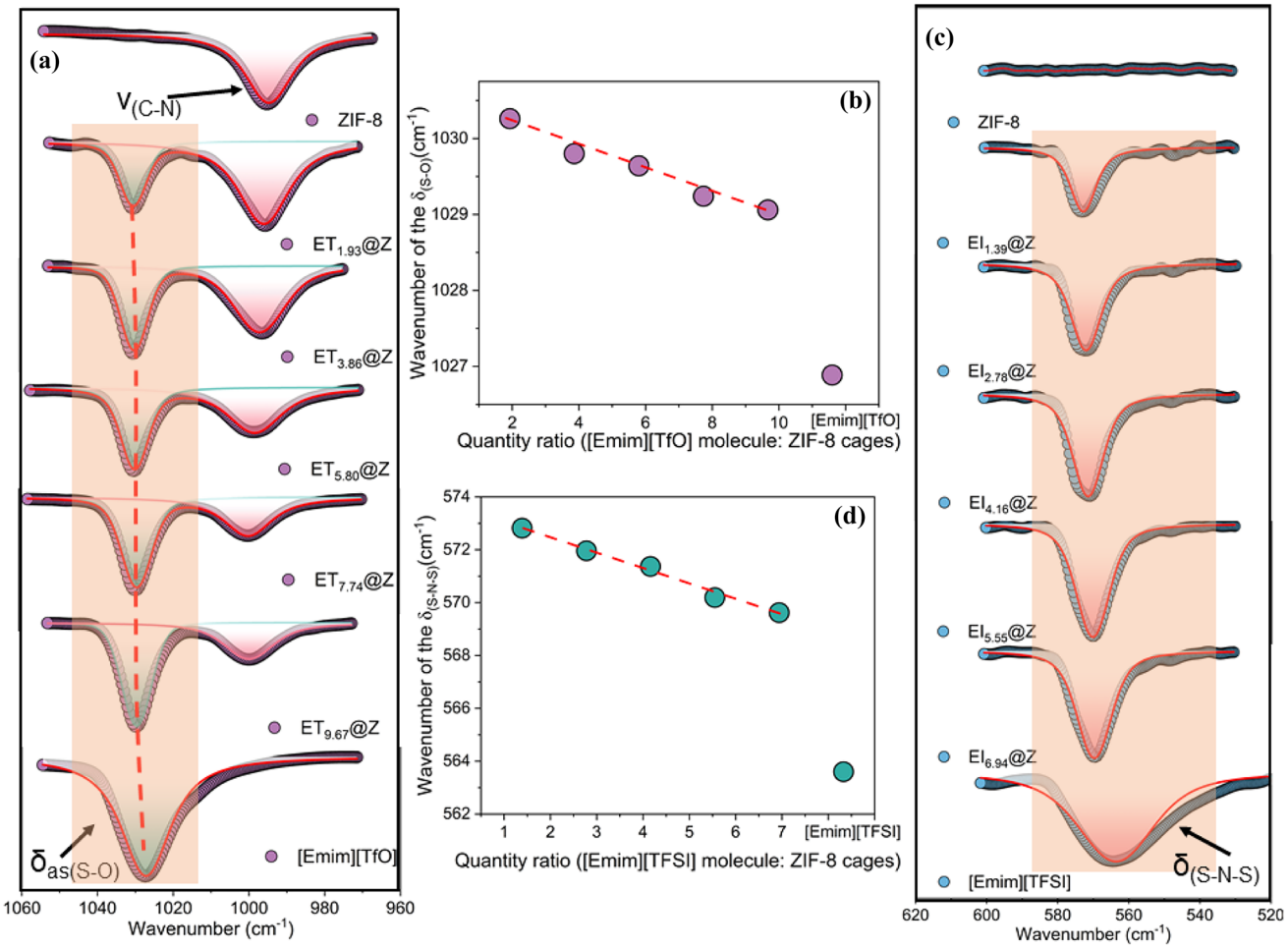

Figure 6 IR spectra of (**a**) $\delta_{as(S-O)}$ of [Emim][TfO] for [Emim][TfO]@ZIF-8 and (**c**) $\delta_{(S-N-S)}$ of [Emim][TFSI] for [Emim][TFSI]@ZIF-8, The peak position related to (**b**) $\delta_{as(S-O)}$ of [Emim][TfO] for [Emim][TfO]@ZIF-8 in the function of the quantity ratio ([Emim][TfO] molecules: ZIF-8 cages) and (**d**) $\delta_{(S-N-S)}$ of [Emim][TFSI] for [Emim][TFSI]@ZIF-8 in the function of the quantity ratio ([Emim][TFSI] molecules: ZIF-8 cages)

as [Emim][TfO] migrates into the ZIF-8 cages, resulting in a weakening of the $-SO_2$ bonding environment. A similar phenomenon can be observed for [Emim][TFSI]. Upon intercalation in ZIF-8, the IR band associated with the bending vibration δ(S–N-S) of the $[TFSI]^-$ anion shifts to a higher wavenumber. This change also reflects the altered bonding dynamics within the confined pores, suggesting weakened ion pair interactions and a modified local environment due to the spatial constraints of the ZIF-8 framework.

The peaks associated with the $\delta_{as}(SO_2)$ and the δ(S–N–S) bending vibration modes become narrower and shift to higher wavenumbers. Such shifts are typically indicative of increased bond strength, often resulting from enhanced bond order or greater polarity [26]. Additionally, the literature suggests that the disruption of hydrogen bonding networks can also cause upward shifts in vibrational frequencies in FT-IR spectra [27, 28]. For example, Wibowo et al. reported that hydrogen bonding leads to the elongation of C=O and N–H bonds due to electrostatic interactions, thereby lowering their vibrational frequencies. In the systems investigated in this study, when an AIL enters the ZIF-8 cages, the bulk AILs environment is initially disrupted. This disruption weakens the intermolecular interactions among the AILs ion pairs, resulting in a strengthening of the $-SO_3$ and S–N–S bonds, which manifests as a shift to higher wavenumbers in the IR spectra. However, as the loading of AILs increases within a single cage, the local environment begins to resemble that of the bulk phase. Consequently, the intermolecular interactions among the AILs molecules

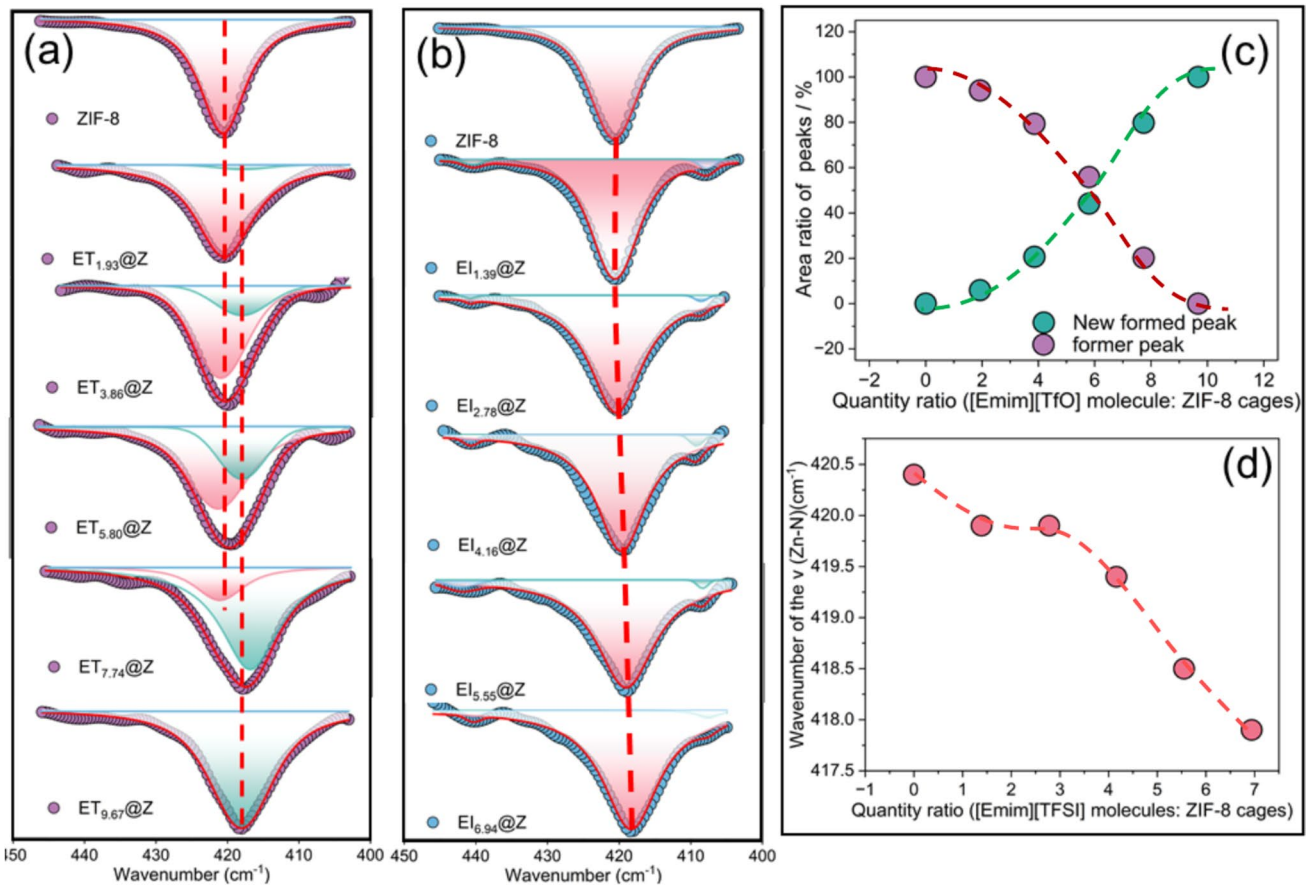

Figure 7 IR spectra of (**a**) [Emim][TfO]@ZIF-8 and (**b**) [Emim][TFSI] relating to Zn-N stretching vibration, (**c**) the area ratio of newly formed peaks and former peaks for $\nu_{(Zn\text{-}N)}$ as a function of the quantity ratio ([Emim][TfO] molecules: ZIF-8 cages), (**d**) the peak position related to $\nu_{(Zn\text{-}N)}$ in the function of the quantity ratio ([Emim][TFSI] molecules: ZIF-8 cages)

are restored, leading to a reduction in bond strength for the -SO_3 and S–N-S functional groups. This results in a subtle redshift of the vibrational bands toward lower wavenumbers.

According to the PXRD refinement results, two distinct mechanisms can be observed for the lattice expansion of ZIF-8 upon intercalation of an AIL. In the case of [Emim][TfO]@ZIF-8, the introduction of the highest loading of [Emim][TfO] that corresponds to 100% loading of the pore volume leads to a significant increase in the lattice constant, reaching a value of 17.361(3) Å for ET9.67@Z. For intermediate loading levels—$ET_{1.93}$@Z, $ET_{3.87}$@Z, $ET_{5.80}$@Z, and $ET_{7.74}$@Z—the system exhibits the coexistence of two distinct cage types: small cages that correspond to pristine ZIF-8 and enlarged cages corresponding to the fully [Emim][TfO]-intercalated structure. As the loading increases, the proportion of enlarged cages grows progressively, while the presence of the original small cages diminishes. In contrast, [Emim][TFSI]@ZIF-8 shows a different behavior. Across all loading levels, only a single type of cage structure is observed, indicating a uniform expansion mechanism. The lattice constants for $EI_{1.39}$@Z, $EI_{2.78}$@Z, $EI_{4.16}$@Z, $EI_{5.55}$@Z, and $EI_{6.94}$@Z are determined to be 17.0303(4), 17.119(1), 17.1641(9), 17.211(6), and 17.223(1) Å, respectively. This monotone and linear increase in lattice constant with increasing [Emim][TFSI] content suggests a homogeneous swelling of the ZIF-8 framework in response to AIL uptake. These two distinct mechanisms demonstrate that the size of the anion and the quantity of AILs' ion pairs play a predominant role in changing the size of the ZIF-8 cages. The BET measurement shows that the ZIF-8 cages can be fully occupied by 4 [Emim][TFSI] ion pairs or 8 [Emim][TfO] ion pairs in Fig. 1. The size of the [TfO] anion is estimated to be 0.305 nm × 0.287 nm × 0.280 nm [29]. The size of the [TFSI] anion is estimated to be

0.298 nm × 0.379 nm × 0.798 nm [30]. Obviously, the length of the [TFSI] anion is much larger than that of the [TfO] anion. Pore blocking occurs when a material occupies interconnected pores, obstructing access to adjacent pores and thereby reducing the accessible surface area and pore volume measured during BET analysis. This effect leads to an underestimation of the actual surface area, as some pores become inaccessible to the adsorbate gas [31–33]. As a result, BET measurements may not align with structural data obtained from techniques such as XRD or IR spectroscopy.

The two distinct lattice-expansion mechanisms can be attributed to differences in both anion size and cation–anion interaction in the two AILs. Kuusik et al. demonstrated that EMIM–TFSI interactions are dominated by delocalized charge distribution rather than localized strong hydrogen bonding, as revealed by combined gas-phase ultraviolet photoelectron spectroscopy (UPS) and density functional theory (DFT) analysis [34]. Wagaye et al. carried out dispersion-corrected DFT (B97D/ωB97X-D) simulation and found interaction energies for $[Emim]^+$–$[TFSI]^-$ conformers to be ~ 41–49 kJ mol^{-1} depending on the geometries, which is below typical strong hydrogen bond energies (~ 50 kJ mol^{-1}), indicating moderate electrostatic/dispersion-dominated interactions rather than strong localized bonding [35]. Anions with a high degree of charge delocalization exhibit weaker electrostatic interactions with cations and typically lower melting points and viscosities. This behavior arises from the distribution of negative charge over multiple atoms, which reduces the effective Coulombic attraction between ions [36, 37]. Accordingly, highly charge-delocalized anions such as $[TFSI]^-$ interact more weakly with imidazolium cations, as the diffuse negative charge diminishes the electrostatic attraction to $[Emim]^+$.

In contrast, smaller anions with more localized charge, such as $[TfO]^-$, engage in stronger cation–anion interactions and exhibit enhanced ion pairing. Tokuda et al. calculated cation–anion interaction energies for imidazolium ionic liquids using MP2/6-311G level ab initio methods. The interaction energy for $[Emim]^+$–$[TFSI]^-$ conformers was found to be ~ − 78.8 kcal mol^{-1}. In comparison, $[Emim]^+$ paired with the smaller, more localized $[TfO]^-$ anion shows a larger-magnitude interaction (~ − 82.6 kcal mol^{-1}), where the more localized negative charge enhances cation–anion association [38]. [Emim][TFSI] has a lower melting point (~ − 16 to − 17 °C) and lower viscosity (~ 34–40 cP at 25 °C) than [Emim][TfO] (~ − 9 °C and ~ 40–70 cP, respectively), which can be attributed to the weaker cation–anion interactions and greater charge delocalization in $[TFSI]^-$. As a consequence of this stronger ion association, [Emim][TfO] preferentially accumulates within a limited number of ZIF-8 cages, giving rise to localized lattice expansion. This results in the coexistence of two distinct cage (expanded cages and original cages), where increasing [Emim][TfO] loading progressively increases the fraction of expanded cages at the expense of the original ones. By comparison, the weaker cation–anion interactions in [Emim][TFSI] promote a more homogeneous distribution of ions throughout the ZIF-8 framework, leading to a uniform and collective expansion of all cages. In this case, a single cage type is observed, with cage dimensions increasing continuously as the [Emim][TFSI] loading increases. This fundamental difference in ion–framework interactions and spatial distribution accounts for the coexistence of two distinct lattice-expansion behaviors observed in the system.

The expansion of the ZIF-8 cages is attributed to flexible apertures that dynamically open through the reorientation of imidazolate linkers induced by guest adsorption, commonly referred to as the 'swing effect [39, 40]. Specifically, the 2-methylimidazole ligands rotate around the Zn-N bonds, leading to the expansion of the cage structure. Evidence supporting this mechanism is provided by IR spectroscopy. The IR peak corresponding to the Zn-N stretching vibration within the ZIF-8 framework exhibits two modes with distinct wavenumbers upon intercalation with different AILs. These differences in vibrational response align well with the structural variations observed in the PXRD refinement results, further confirming the influence of AILs on the dynamic behavior of the ZIF-8 framework. For [Emim][TfO]@ZIF-8, the introduction of the highest loading of [Emim][TfO] results in a pronounced shift in the Zn-N stretching vibration band to a lower wavenumber, reaching 417.9 cm^{-1} for $ET_{9.67}$@Z. At intermediate loadings, $ET_{1.93}$@Z, $ET_{3.87}$@Z, $ET_{5.80}$@Z, and $ET_{7.74}$@Z, two distinct Zn-N stretching modes coexist, appearing at 420.4 cm^{-1} and 417.9 cm^{-1}, indicating a phase mixture of unmodified and expanded ZIF-8 cages. In contrast, [Emim][TFSI]@ZIF-8 exhibits a different trend. Across all loading levels, only a single Zn-N stretching mode is observed, which progressively shifts to lower wavenumbers with increasing [Emim][TFSI] content. Specifically, the Zn-N stretching bands appear at 419.9 cm^{-1}, 419.4 cm^{-1},

418.9 cm^{-1}, 418.4 cm^{-1}, and 417.9 cm^{-1} for $EI_{1.39}$@Z, $EI_{2.78}$@Z, $EI_{4.16}$@Z, $EI_{5.55}$@Z, and $EI_{6.94}$@Z, respectively. This continuous shift suggests a uniform expansion mechanism across the ZIF-8 framework.

It is presumed that the internal pressure exerted by AILs molecules confined within the pores of ZIF-8 leads to an elongation of the Zn-N bond lengths relative to their original values. This structural change is supported by the findings of He et al. [41], who demonstrated that the elongation of specific bond lengths is typically associated with a corresponding shift to lower wavenumbers in vibrational spectra. Similarly, Verma et al. [42] synthesized a $BiFeO_3$ nanoparticles vis sol–gel auto-combusion method and reported a shift in the vibrational band of the Fe–O bond from 560 to 554.5 cm^{-1}, which was attributed to an increase in Fe–O bond length. This red shift was linked to a decrease in the bond's force constant, indicating a weakening of the bond. Consequently, the weakened Fe–O bond becomes more responsive to lower-energy vibrational modes [43].

The ZIF-8 structural model proposed by Yu et al. [44] provides a useful framework to discuss this phenomenon, as illustrated in Fig. 8. Based on DFT calculations, five distinct aperture configurations with varying effective diameters were identified: pristine (d = 3.4 Å), closed (d = 4.1 Å), semi-open (d = 4.2 Å), open (d = 4.7 Å), and fully open (d = 6.9 Å). The descriptors "closed," "semi-open," and "open" refer to the conformational status of the six imidazolate linkers surrounding each cage window—ranging from all six rings being in the closed position to configurations with three or all six rings rotated into open conformations. These differences arise from the rotational flexibility of the 2-methylimidazole ligands, which leads to variations in aperture size and cage volume. In our study, the observed expansion of ZIF-8 cages is most probably attributed to the internal pressure exerted by the intercalated AILs ion pairs. Presumably, the [Emim][TfO]@ZIF-8 composite displays two types of cage configurations, corresponding to partially and fully expanded states, as shown in Fig. 8a and b. In contrast, the [Emim][TFSI]@ZIF-8 composite may exhibit a broader distribution of structural states, incorporating all five aperture configurations as illustrated in Fig. 8a and c–f. This discrepancy is likely due to the larger size and elongated structure of the $[TFSI]^-$ anion, which imposes a greater steric demand and promotes a wider range of cage expansions within the ZIF-8 framework. Presumably, the combined effects of the swing motion of 2-methylimidazole ligands and the elongation of Zn-N bonds contribute to the expansion of ZIF-8 cages upon intercalation of AILs, such as [Emim][TfO] and [Emim][TFSI], within the ZIF-8 framework.

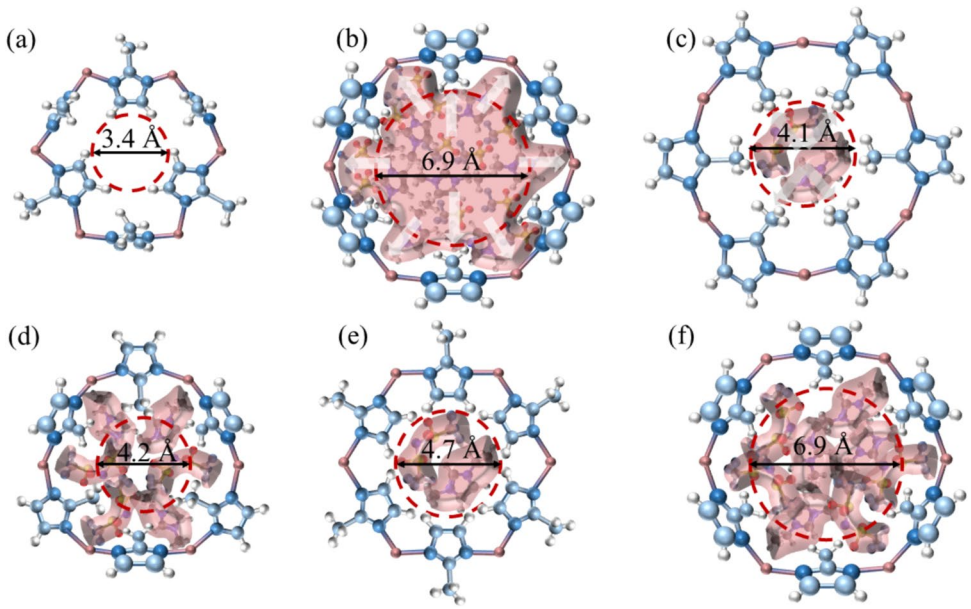

Figure 8 Six different aperture structures with different aperture diameters after loading different AILs (**a**) pristine, (**b**) 10 [Emim][TfO] ion pairs, (**c**) 1 [Emim][TFSI] ion pairs, (**d**) 2 [Emim][TFSI] ion pairs, (**e**) 3 [Emim][TFSI] ion pairs, (**f**) 4 [Emim][TFSI] ion pairs

Conclusion

In this study, two AILs, [Emim][TfO] and [Emim][TFSI], were successfully intercalated in the porous framework of ZIF-8. Structural analysis revealed two distinct mechanisms of lattice expansion. For [Emim][TfO]@ZIF-8, a two-phase system with coexisting lattice constants was observed, indicating a sudden phase transition during the incorporation process. In contrast, [Emim][TFSI]@ZIF-8 exhibited a single-phase structure with a gradual and continuous lattice expansion as the loading increased. These structural modifications are attributed to the rotational flexibility of the 2-methylimidazole linkers and the elongation of Zn–N bonds, both driven by internal pressure from the encapsulated AILs. Moreover, confinement within the ZIF-8 cages disrupts the bulk ionic environment, enhancing the strength of the $-SO_3$ and S–N-S bonds, as evidenced by the sharp and blue-shifted vibrational modes in the IR spectra. These findings offer valuable insights into host–guest interactions in AIL@MOF systems and provide a strategic basis for tailoring MOF properties through AIL intercalation.

Owing to the immobilization of AILs within MOF frameworks, the incorporation of lithium salts enables these composites to function as solid-state electrolytes that support Li^+ migration through the interconnected MOF cages. AILs exhibit high solubility for lithium salts, allowing the salts to dissolve uniformly within the AIL phase. Upon encapsulation of the lithium-salt-containing AIL inside the MOF structure, continuous ion-conduction pathways are established while maintaining the solid-state integrity of the material. These combined characteristics underscore the strong potential of AIL–MOF composites as safe, high-performance electrolytes for MOF-based solid-state lithium batteries and other advanced electrochemical energy-storage devices. In contrast, PILs are unsuitable as lithium battery electrolytes because their intrinsic protonic nature leads to hydrogen evolution and electrochemical instability at lithium electrodes. Beyond energy-storage applications, AIL–MOF composites also exhibit significant promise for gas absorption and separation, particularly for CO_2 capture, by uniting the high gas solubility of AIL with the molecular sieving capability and intrinsic selectivity of MOF frameworks.

Acknowledgements

We would like to appreciate the China Scholarship Council for the International Cooperative Training Project for Innovative Talents (project No.: CXXM2011280411). We gratefully acknowledge K. Klafki and A. Everwand for technical support. Open Access publication funded by the Deutsche Forschungsgemeinschaft (DFG, German Research Foundation)—Grant No. 491111487.

Funding

Open Access funding enabled and organized by Projekt DEAL.

Supplementary Information The online version contains supplementary material available at https://doi.org/10.1007/s10853-026-12380-0.

References

[1] Duan C, Liang K, Zhang Z, Li J, Chen T, Lv D, Li L, Kang L, Wang K, Hu H, Xi H (2022) Nano Mater Sci 4:351–365
[2] Furukawa H, Cordova KE, O'Keeffe M, Yaghi OM (2013) Science 341:1230444
[3] Jiao L, Seow JYR, Skinner WS, Wang ZU, Jiang H-L (2019) Mater Today 27:43–68
[4] Deng J-H, Luo J, Mao Y-L, Lai S, Gong Y-N, Zhong D-C, Lu T-B (2020) Sci Adv 6:1–8

[5] Zuluaga S, Canepa P, Tan K, Chabal YJ, Thonhauser T (2014) J Phys Condens Matter 26:133002
[6] Han X, Yang X, Yu C, Lu S, Pouya ES, Bai P, Lyu J, Guo X (2021) CrystEngComm 23:3026–3032
[7] Sharma P, Sharma S, Kumar H (2024). J Mol Liq. https://doi.org/10.1016/j.molliq.2023.123447
[8] Greaves TL, Weerawardena A, Fong C, Krodkiewska I, Drummond CJ (2006). J Phys Chem B. https://doi.org/10.1021/jp0634048
[9] Greaves TL, Drummond CJ (2008) Chem Rev 108:206–237
[10] Hayes R, Imberti S, Warr GG, Atkin R (2013) Angew Chem Int Ed Engl 52:4623–4627
[11] Stoimenovski J, Izgorodina EI, MacFarlane DR (2010) Phys Chem Chem Phys 12:10341–10347
[12] Thawarkar S, Khupse ND, Kumar A (2016) ChemPhysChem 17:1006–1017
[13] Fox ET, Paillard E, Borodin O, Henderson WA (2012) J Phys Chem C 117:78–84
[14] Fernicola A, Navarra MA, Panero S (2008) J Appl Electrochem 38:993–996
[15] Dehdashtian S, Pourreza N, Rostamnia S (2022). Microchem J. https://doi.org/10.1016/j.microc.2022.107839
[16] Zhang Z, Li C, Chandresh A, Heinke L (2021) Ionics 28:487–494
[17] Su L, Han W, Si F, Yue W, Li F, Zhou X, Wang C, Fu H (2023) J Ind Eng Chem 121:393–400
[18] Shekhah O, Swaidan R, Belmabkhout Y, du Plessis M, Jacobs T, Barbour LJ, Pinnau I, Eddaoudi M (2014) Chem Commun Camb 50:2089–2092
[19] Cho B-S, Choi J, Kim K-Y (2017) Fibers Polym 18:1452–1458
[20] Wei Y, Chen W, Ge X, Liang J, Xing Z, Zhang Q, Wang Z-X (2023). Polymer. https://doi.org/10.1016/j.polymer.2023.126501
[21] Doebelin N, Kleeberg R (2015) J Appl Crystallogr 48:1573–1580
[22] Wojdyr M (2010) J Appl Crystallogr 43:1126–1128
[23] Singh DK, Rathke B, Kiefer J, Materny A (2016) J Phys Chem A 120:6274–6286
[24] Dhumal NR, Noack K, Kiefer J, Kim HJ (2014) J Phys Chem A 118:2547–2557
[25] Cheng P, Hu YH (2014) J Phys Chem C 118:21866–21872
[26] Bassey VM, Apebende CG, Idante PS, Louis H, Emori W, Cheng CR, Agwupuye JA, Unimuke TO, Wei K, Asogwa FC (2022) J Fluoresc 32:1005–1017
[27] Yang Y, Ye Z, Liu X, Su J (2020) J Mater Chem C 8:5280–5292
[28] Kalhor P, Xu J, Ashraf H, Cao B, Yu ZW (2020) J Phys Chem B 124:1229–1239
[29] Fan J, Xiao Q, Fang Y, Li L, Yuan W (2018) Ionics 25:1303–1313
[30] Lee S-Y, Ogawa A, Kanno M, Nakamoto H, Yasuda T, Watanabe M (2010) J Am Chem Soc 132:9764–9773
[31] Vishnyakov A, Neimark AV (2003) Langmuir 19:3240–3247
[32] Weidenthaler C (2011) Nanoscale 3:792–810
[33] Islamoglu T, Idrees KB, Son FA, Chen Z, Lee S-J, Li P, Farha OK (2022) J Mater Chem A 10:157–173
[34] Kuusik I, Kook M, Pärna R, Kivimäki A, Käämbre T, Reisberg L, Kikas A, Kisand V (2019). J Mol Liq. https://doi.org/10.1016/j.molliq.2019.111580
[35] Wagaye AM, Yohannes T, Workneh GA (2024) Dis Appl Sci 5:63
[36] Pradhan A, Ravi PR, Sonone PR, Chourasia MK, Singh Y (2025). ChemSelect. https://doi.org/10.1002/slct.202504298
[37] Egorova KS, Gordeev EG, Ananikov VP (2017) Chem Rev 117:7132–7189
[38] Tsuzuki S, Tokuda H, Hayamizu K, Watanabe M (2005) J Phys Chem B 109:16474–16481
[39] Tanaka S, Fujita K, Miyake Y, Miyamoto M, Hasegawa Y, Makino T, Van der Perre S, Cousin Saint Remi J, Van Assche T, Baron GV, Denayer JFM (2015) J Phys Chem C 119:28430–28439
[40] Hobday CL, Bennett TD, Fairen-Jimenez D, Graham AJ, Morrison CA, Allan DR, Duren T, Moggach SA (2018) J Am Chem Soc 140:382–387
[41] He X, Ni Y, Hou Y, Lu Y, Jin S, Li H, Yan Z, Zhang K, Chen J (2021) Angew Chem Int Ed Engl 60:22672–22677
[42] Verma R, Chauhan A, Batoo KM, Kumar R, Hadhi M, Raslan EH (2021) Ceram Int 47:3680–3691
[43] Behera B, Das PK (2018) J Phys Chem A 122:4481–4489
[44] Yu T, Cai Q, Lian G, Bai Y, Zhang X, Zhang X, Liu L, Zhang S (2021). Chem Eng J. https://doi.org/10.1016/j.cej.2021.129638